# Supporting Information

**Oriented Arrays of $Co_3O_4$ Nanoneedles for Highly Efficient Electrocatalytic Water Oxidation**

*Jun-Jun Zhang[a], Tian-Jian Zhao[a], Hong-Hui Wang[a], Yun-Xiao Lin[a], Guang-Yao Zhai[a], Zhi-Dong Jiang[a]*, Xin-Hao Li[a]*, Shin-Ichi Hirano[b], and Jie-Sheng Chen[a]*

[a] School of Chemistry and Chemical Engineering, Shanghai Jiao Tong University, Shanghai 200240, P. R. China.

[b] Hirano Institute for Materials Innovation, Shanghai Jiao Tong University, Shanghai 200240, P. R. China.

*To whom correspondence should be addressed

**Correspondence to:**

xinhaoli@sjtu.edu.cn (Xin-Hao Li)

zdjiang@sjtu.edu.cn (Zhi-Dong Jiang).

# List of Contents

chemical compositions and oxidation states of the Ti@*m*-$Co_3O_4$ before and after 12h stability test.

**Figure S18.** Typical SEM images the Ti@*m*-$Co_3O_4$ after 12h stability test. The optimal synthesis condition gave a material that is denoted hereafter as Ti@*m*-$Co_3O_4$, unless indicated otherwise.

**Figure S19.** Typical EDS mapping of the Ti@*m*-$Co_3O_4$ after 12h stability test.

**Figure S20.** Typical TEM image the Ti@*m*-$Co_3O_4$ after 12h stability test. The optimal synthesis condition gave a material that is denoted hereafter as Ti@*m*-$Co_3O_4$, unless indicated otherwise.

**Figure S21.** XRD of the initial Ti@*m*-$Co_3O_4$ and used after 12h stability test.

## 3. Supplementary Tables:

**Table S1.** Summarized the relevant synthesis parameters of Ti@*p*-$Co_3O_4$ and Ti@*m*-$Co_3O_4$ (x= 10, 20, and 30min) hybrid electrodes.

**Table S2.** Comparison of OER catalytic performance for Ti@*p*-$Co_3O_4$ and Ti@*m*-$Co_3O_4$ (x= 10, 20, and 30min) hybrid electrodes in neutral solution (pH = 7).

**Table S3.** Comparison of the OER performance of well-developed electrocatalysts under neutral solution and near neutral solution.

**Table S4.** Comparison of catalytic performances (TOF) and conditions for a variety of earth-abundant transition metals electrocatalysts in neutral solution and near neutral condition.

**Table S5.** Comparison of electrochemical double-layer capacitance ($C_{dl}$) for Ti@*p*-$Co_3O_4$ and Ti@*m*-$Co_3O_4$ hybrid electrocatalysts in neutral solution (pH = 7).

## 4. Notes and references

# 1. Experimental Section

## 1.1 Preparation of Ti@$Co(CO_3)_{0.5}OH$ nanoneedles array electrode

All chemicals are of analytical grade and were used as received without further purification. The Ti mesh substrate was obtained by cutting the commercial Ti mesh into rectangle shape (4 cm × 1 cm). The average mass loading was 26.86 mg $cm^{-2}$ for Ti mesh. Prior to the reaction, Ti mesh was washed with HCl, ethanol and water several times to remove the surface impurities. The Ti@$Co(CO_3)_{0.5}OH$ nanoneedles array were grown on the Ti mesh via a previously reported method. In a typical procedure, Cobaltous nitrate hexahydrate, $Co(NO_3)_2 \cdot 6H_2O$ (1.5mmol, 0.436g; 99.5%, Adamas-beta®), Urea, $CH_4N_2O$ (7.5mmol, 0.45g; 99.5%, Aladdin) and Ammonium fluoride, $NH_4F$ (4mmol, 0.148g; 99.5%, Aladdin) were dissolved in 25 mL of deionized water (18.2 MΩ·cm) were added to a 50 mL Teflon-lined autoclave with vigorous stirring for 60 min. Ti mesh (Hongshan District, Wuhan Instrument Surgical Instruments business.) was put in the polytetrafluoroethylene-lined stainless-steel autoclave and placed at an angle against the wall of the Teflon liner. The autoclave was sealed and maintained at 120°C for 4h and cooled down naturally to room temperature. Subsequently, the electrodes were rinsed with deionized water and absolute ethanol several times to remove any ionic residual, and then dried in vacuum at 80°C for 12h The collected sample from the bottom of Teflon-lined autoclave was marked as *p*-$Co_3O_4$.

## 1.2 Preparation of Ti@*p*-$Co_3O_4$ nanoneedles array and hydrazine-treated ($N_2H_4 \cdot H_2O$) nanoarrays electrodes

The resulting precursor Ti@$Co(CO_3)_{0.5}OH$ nanoneedles array was further annealed at 350 °C, 2h in air to convert into Ti@$Co_3O_4$ nanoneedles array electrode. The loading of $Co_3O_4$ nanoneedles array on the Ti mesh was estimated through inductively coupled plasma (ICP). The loading amount of the $Co_3O_4$ nanoneedles array was 0.843mg $cm^{-2}$. We used 0, 10, 20 and 30min hydrazine-treated time for comparison. To obtain the hydrazine-treated electrode, the Ti@*p*-$Co_3O_4$ nanobundles array electrode was immersed into dilute hydrazine ($V_{hydrazine}$:$V_{deionized\ water}$ = 3:1) under different time (10, 20, 30min). The optimal synthesis condition gave a material that is denoted hereafter

as Ti@*m*-$Co_3O_4$, unless indicated otherwise. Relevant parameters were listed in Table S1 and S2. The final electrodes were marked as Ti@*m*-$Co_3O_4$-x, where "x" represents the different hydrazine-treated time for samples (x = 10, 20, 30). The optimal synthesis condition (20min) gave a material that is denoted hereafter as Ti@*m*-$Co_3O_4$, unless indicated otherwise. Meanwhile, the initial nanoneedles array, without hydrazine-treated, was recorded as Ti@*p*-$Co_3O_4$. Relevant parameters were listed in Table S1 and S2. The Ti@*m*-$Co_3O_4$ and Ti@*p*-$Co_3O_4$ nanoneedles could be used as an integrated electrode for the electrolysis tests. The hydrazine-treated collected *p*-$Co_3O_4$ sample was marked as *m*-$Co_3O_4$.

### 1.3 Preparation of Ti + $IrO_2$ electrode

The Ti +$IrO_2$ electrode was prepared by dropping the $IrO_2$ catalyst ink on a Ti mash substrate. To prepare $IrO_2$ loaded electrodes, 5 mg $IrO_2$ and 80 μL 5 wt% Nafion solution were dispersed in 350μL water and 700μL ethanol mixed solvent by 8h sonication to form an homogeneous ink. Then, 530 μL catalyst ink was loaded on a preprocessed Ti mesh (1*3 $cm^2$).

### 1.4 Material characterizations

The Powder X-ray diffraction (XRD) patterns were recorded on a Bruker D8 Advance X-ray diffractometer with Cu-Kα radiation (λ = 1.5418 Å) with a scan rate of 6° $min^{-1}$. The SEM measurements were performed on a FEI Nova Nano SEM 2300. The TEM and HRTEM measurements were taken with a JEM-2100F microscope operated at an acceleration voltage of 200 kV. The X-ray photoelectron spectroscopy (XPS) measurements were conducted on a Kratos Axis Ultra DLD spectrometer. The XPS peaks were calibrated through the C 1s before the relevant comparison. The inductively coupled plasma (ICP) measurements were conducted on a Perkin-Elmer Optima 3300DV ICP spectrometer for the loading analysis. Raman microprobe spectroscopy was performed on Thermo Fisher DXR, Waltham, MA, USA with excitation wavelength 532 nm. The UV–vis absorption spectra were recorded on Shimadzu UV-2450 UV–vis spectrophotometer. The X-ray absorption find structure (XAFS) spectra of the samples were collected beamline BL14W1 of the shanghai synchrotron radiation facility.

### 1.5 Electrochemical characterizations

Electrochemical measurements are performed with a CHI 730C electrochemistry workstation (CH Instruments, Inc., Shanghai) in a standard three-electrode system. The three-electrode electrochemical cell was consisted of a saturated calomel electrode (SCE), Ti@m-$Co_3O_4$ nanoneedles array, graphite rod, served as reference electrode, working electrode, counter electrode, respectively. A saturated calomel electrode (SCE) was used as the reference electrode for all the electrochemical tests and the potential was calibrated to a reversible hydrogen electrode (RHE) (the potential of the SCE as 0.241 V vs. RHE). Commercial $IrO_2$ catalyst was used as a reference for evaluating the OER performances of all the Ti@m-$Co_3O_4$ electrodes.

Prior to all experiments, the electrolyte was purged with $O_2$ gas to saturate. Polarization curves measurements were conducted in 1 M phosphate buffer saline solution (PBS) with a scan rate of 10mV $s^{-1}$. The long-term durability test was performed using chronoamperometric measurements. The cyclic voltammogram (CV) 1000 cycles durability test was conducted by potential cycling from 1.4 to 1.8 V vs. RHE. The scan rate for cycling was fixed at 50 mV $s^{-1}$. Double layer capacitance measurements were conducted by varying the scan rates (100-200 mV $s^{-1}$ with an interval 20 mV) in a potential window without Faradaic process. To reflect the real catalytic currents, all polarization curves corresponding shown in this paper were calibrated after i*Rs correction. $E\ corrected = E\ measured - i*Rs$ (where *Ecorr* is the i*Rs-compensated potential, *Emea* is the experimentally measured potential, and *Rs* is the resistance, respectively.) Electrochemical impedance spectroscopy (EIS) is a general method for inquiring the electron and mass transfer kinetics in the electrochemical process. The EIS measurements for the Ti@p-$Co_3O_4$ and Ti@m-$Co_3O_4$ were performed in $O_2$-saturated 1.0 M PBS solutions at a bias voltage of 1.5 V vs. RHE using a graphite rod as the counter electrode with the frequency range from $10^5$ Hz to 0.1 Hz. The turnover frequency (TOF) is defined as the number of $H_2$ or $O_2$ molecules generated per site per second: TOF = j/(n*F*N), where j is the measured current density (A $cm^{-2}$), n is the mole number of electrons per mole of $O_2$, F is the Faraday constant, 96485 C/mol, and N is the content of the catalyst (mol $cm^{-2}$). All measurements were conducted at room

temperature. The current density mentioned in this study was based on geometric surface area. To promote the mass transport in the process of i-t measurement, the electrolyte was vigorously stirred by an electromagnetic mixing.

# 2. Supplementary Figures:

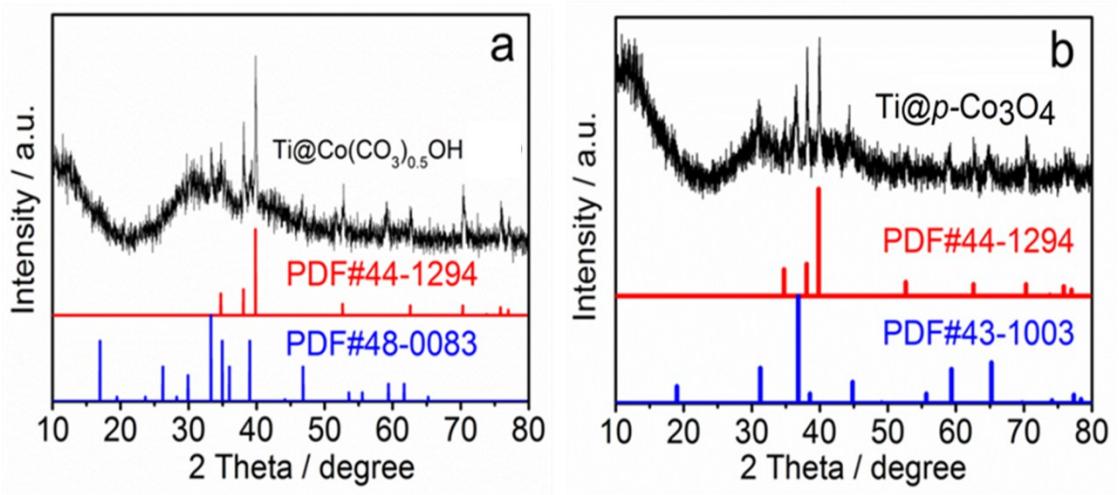


**Figure S1.** XRD patterns of obtained Ti@$Co(CO_3)_{0.5}(OH)$ nanoneedles array, Ti@*p*-$Co_3O_4$. Recently, growing attention has been given to spinel-type materials because spinels have octahedral sites (which are widely accepted as the catalytically active sites) as in previous report. All of the observed diffraction peaks can be perfectly indexed to the standard. As revealed in Figure S1a, the precursors of the nanoneedles are identified as orthorhombic (PDF# 48-0083) without any evidence of impurities. After thermal treatment (350$^{o}$C, 2h), the $Co(CO_3)_{0.5}(OH)$ nanoneedles precursors absolutely transformed into the spinel $Co_3O_4$ nanoneedles (JCPDS card 42-1467, Figure S1b).

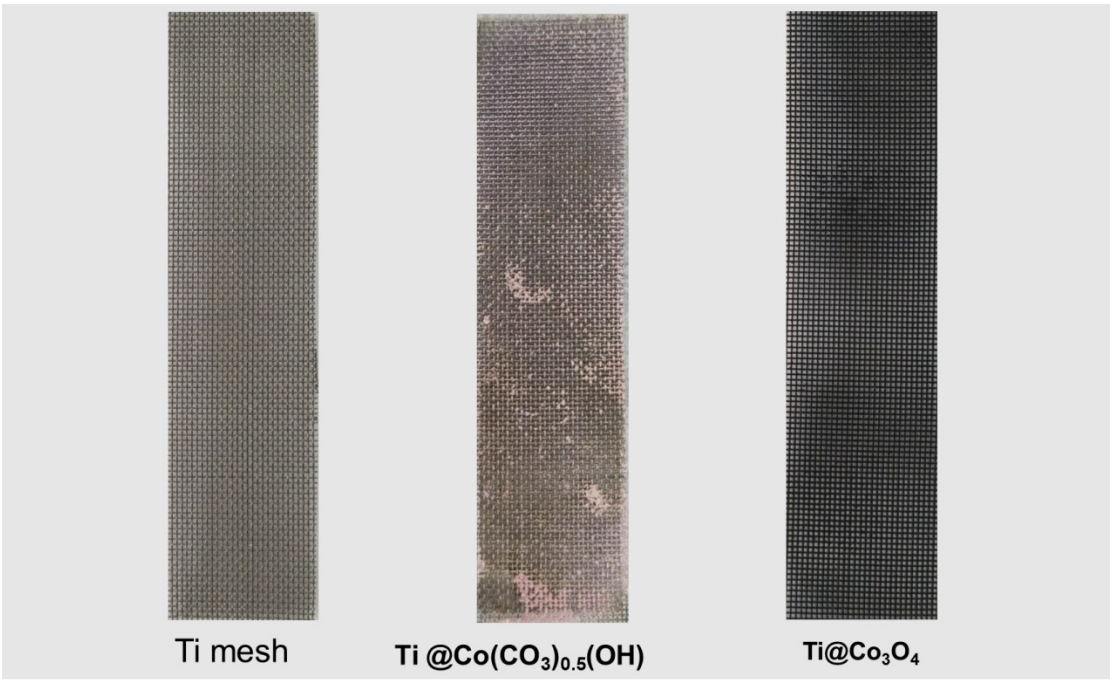


**Figure S2.** The photograph of bare Ti mesh, Ti@$Co(CO_3)_{0.5}(OH)$ nanoneedles array electrode and pristine Ti@*p*-$Co_3O_4$ during the synthetic process. With the synergetic effect of the Ti mesh, abundant nanoarray, Ti@$Co_3O_4$ may exhibits superior electrocatalytic activity, and long-term stability, as compared to the commercial $IrO_2$ catalyst. The amount of powder catalyst is limited on glassy carbon electrode due to weak affinity and restricted area. Benefiting from the strong active site–substrate interaction, the Ti@*m*-$Co_3O_4$ electrode could afford a high mass loading and thus exceptionally high stability and current density.

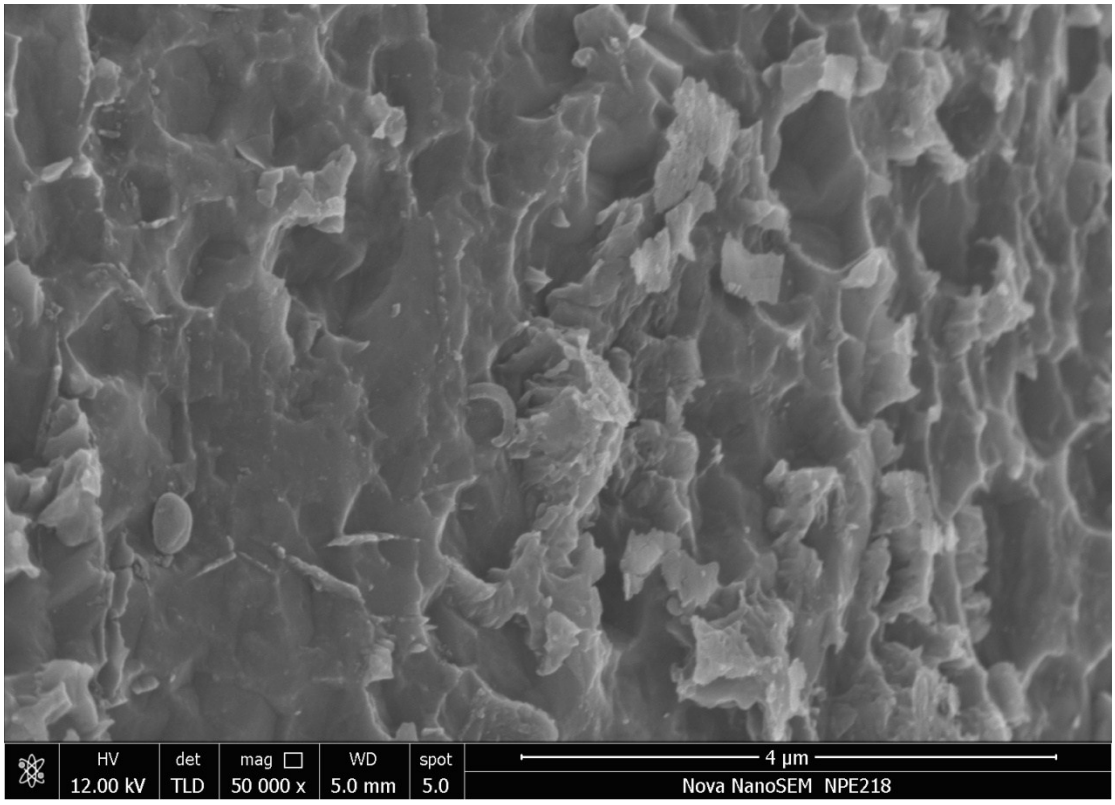


**Figure S3.** FE-SEM image of bare Ti mesh. The titanium mesh was fabricated from titanium wire with a diameter about 100 µm. The Ti mesh with bumpiness surface facilitates the directional growth of catalyst, exposing abundant active sites of the electrode for electrochemical reactions at the electrode and electrolyte interface. These efficacious characteristics make metalline titanium mesh display excellent support material for electrochemical processes.

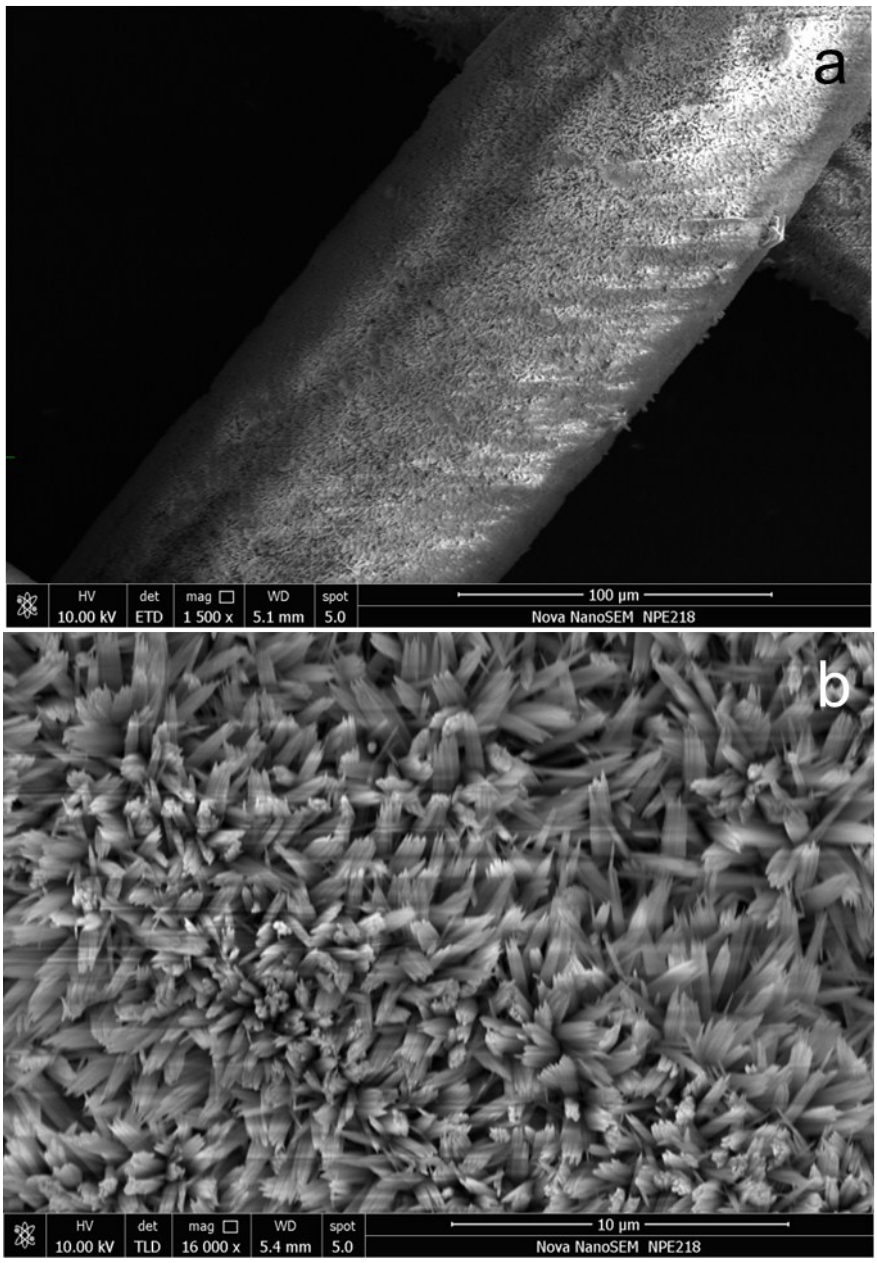


**Figure S4.** The SEM images of the Ti@$Co(CO_3)_{0.5}(OH)$ arrays electrode.

Figure S4 show TEM images of the Ti@$Co(CO_3)_{0.5}(OH)$, which exhibited a 3D array structure. The $Co(CO_3)_{0.5}(OH)$·nanoarrays are densely and vertically formed on the Ti mesh substrate.

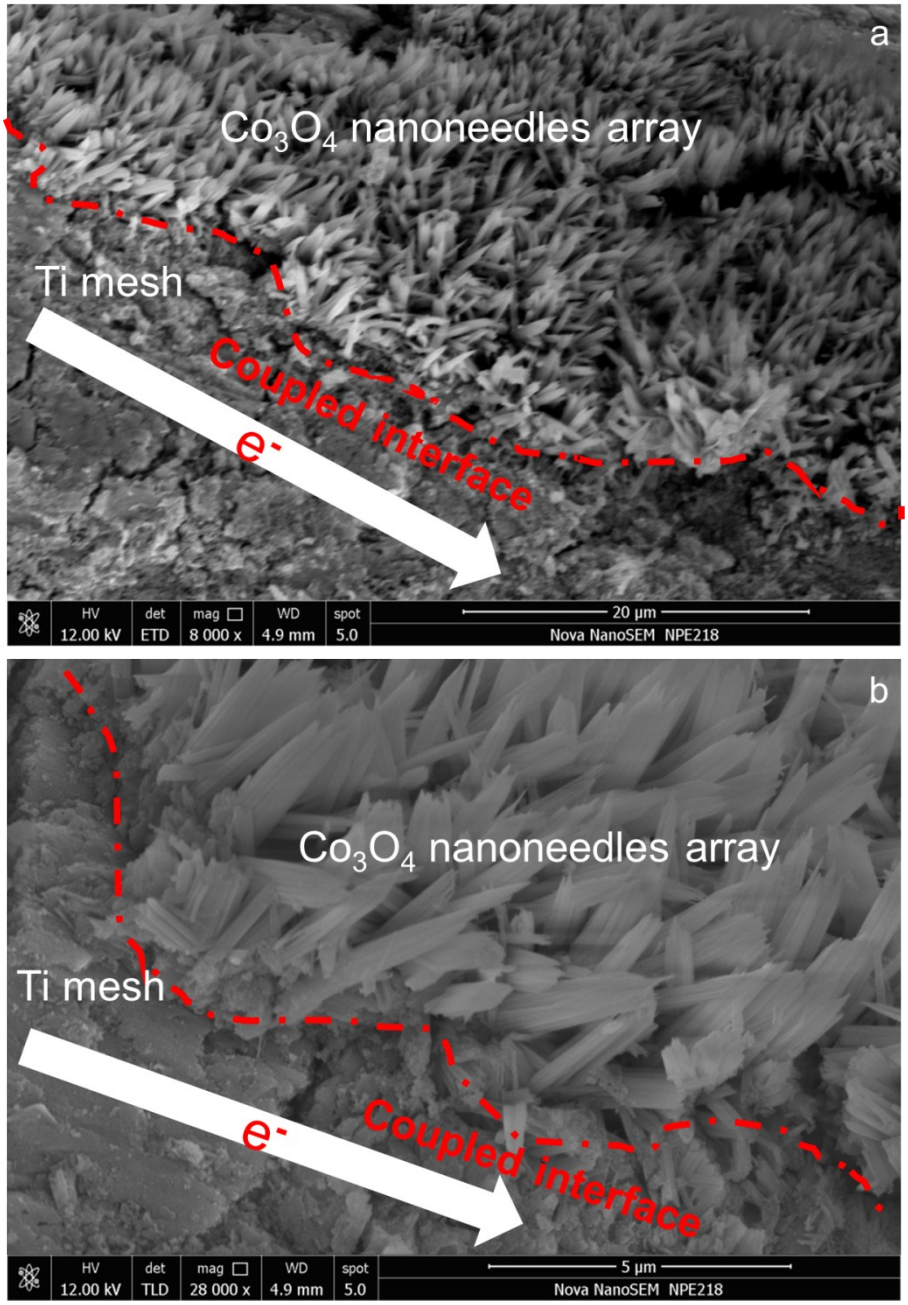


**Figure S5.** The SEM images of the Ti@*m*-$Co_3O_4$ (hydrazine-treated) nanoneedles array electrode. Figure 1b shows the SEM images of the Ti@$Co_3O_4$ after hydrazine treatment for 20min. The Ti@*m*-$Co_3O_4$ electrode with closely interconnected nanoarrays structure is beneficial for shortening the electron transfer pathway and providing a large surface area and active sites. This unique structure coupled interface endow $Co_3O_4$ nanoneedles good electrocatalytic properties. Low tortuosity of the hybrid electrode is critical for efficient mass transfer during the gas generation reaction. The hierarchical Ti@*m*-$Co_3O_4$ electrode electrode exhibits a remarkable electrocatalytic activity and durability with a low overpotential.

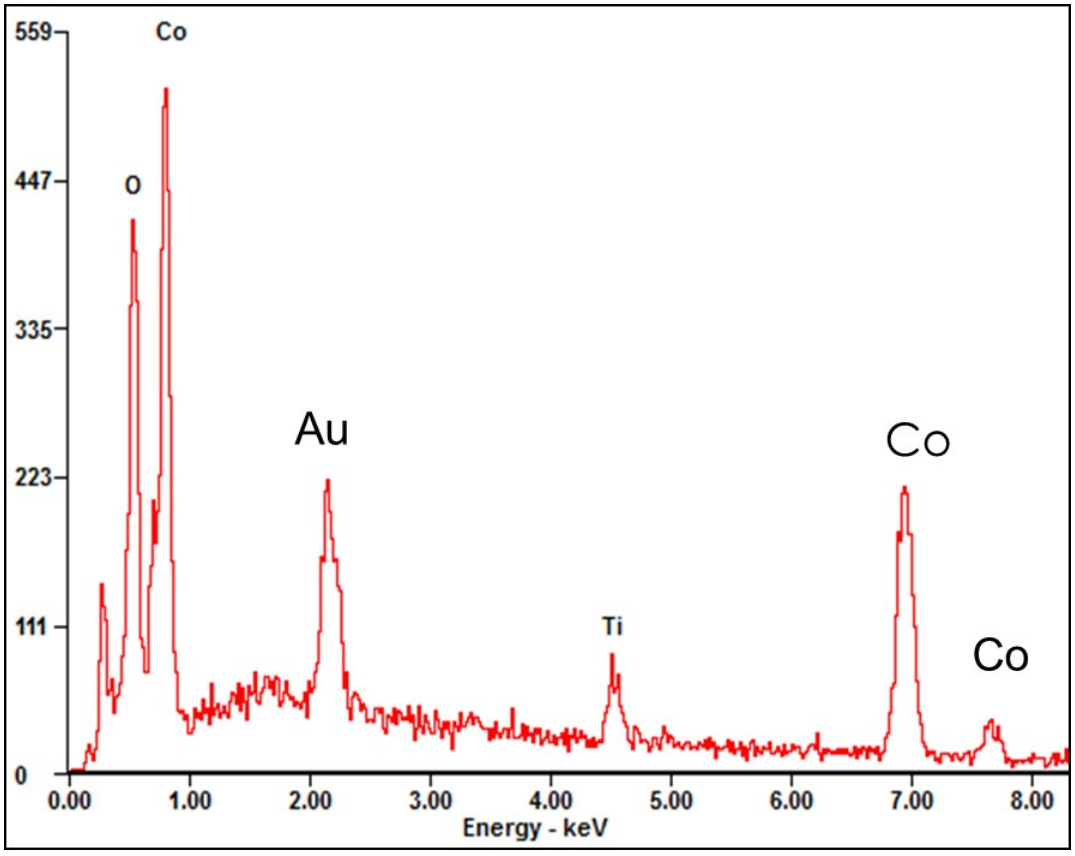


**Figure S6.** EDX spectrum of Ti@*m*-$Co_3O_4$ nanoneedles array (20min hydrazine-treated Ti@*m*-$Co_3O_4$). The Au signal is originated from the sputtered Au before test. The Ti signal is originated from the Ti mesh substrate.

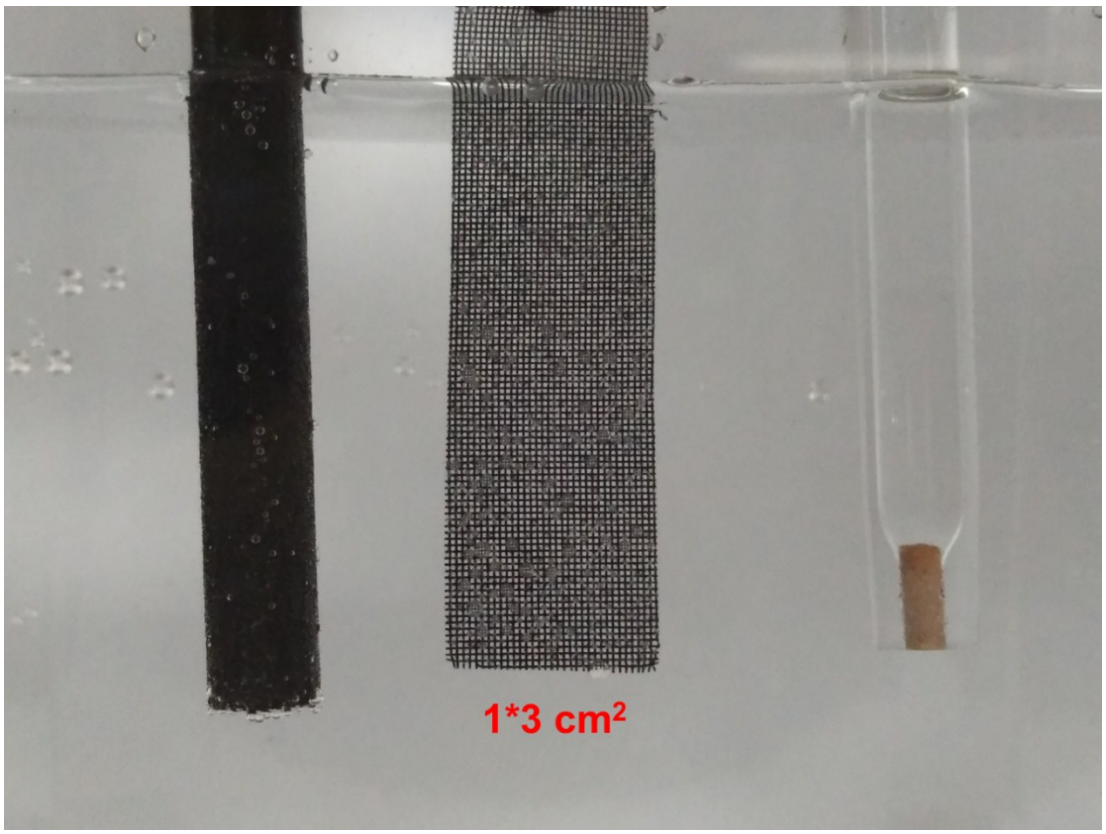


**Figure S7.** The photograph of standard three-electrode configuration during OER process in $O_2$-saturated 1 M PBS aqueous solution. The three-electrode electrochemical cell was consisted of a Ti@*m*-$Co_3O_4$ nanoneedles array electrocatalyst (working electrode), a graphite rod (counter electrode) and a saturated calomel electrode (SCE, reference electrode). The growth of active materials ($Co_3O_4$ nanoneedles array) on Ti mesh can greatly enhance the water splitting efficiency. Electrochemical tests require effective immobilization of nanocatalysts on conductive substrates, as current collectors by using a polymer binder like Nafion. However, the polymer binder will increase the resistance and block the active sites and thus inhibit mass diffusion, leading to reduced catalytic activity. The substrate Ti mesh possess a high conductivity and chemically inert can be used in both acidic, neutral and alkaline media, serving as an ideal support for OER.

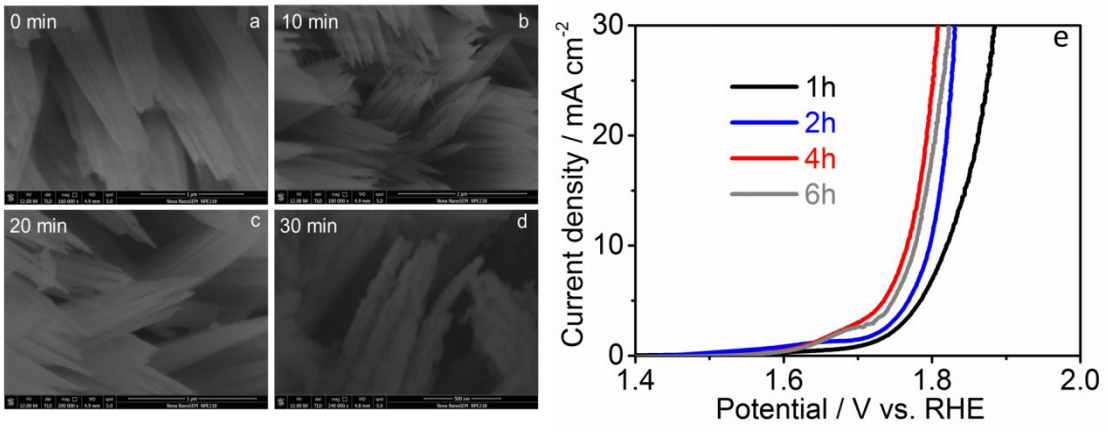


**Figure S8.** The SEM images of the Ti@*p*-$Co_3O_4$ and Ti@*m*-$Co_3O_4$ nanoneedles array with a hydrazine treatment time of (a) Ti@*p*-$Co_3O_4$ (0min), (b) 10min, (c) 20min and (d) 30min, respectively. (e) The LSV curves of Ti@*p*-$Co_3O_4$ electrodes with different hydrothermal reaction time. The effect of hydrazine-treated time on the OER performance for $Co_3O_4$ nanoneedles array was also systematically studied. The 30min sample showed low crystallinity with loose morphology and excessive amount of porous, which can be attributed to the excess time of hydrazine treatment. The time of hydrazine treatment was optimized to be 20min in current research. The result directly demonstrates the pivotal role of hydrazine treatment with appropriate degree in maintaining the excellent performance.

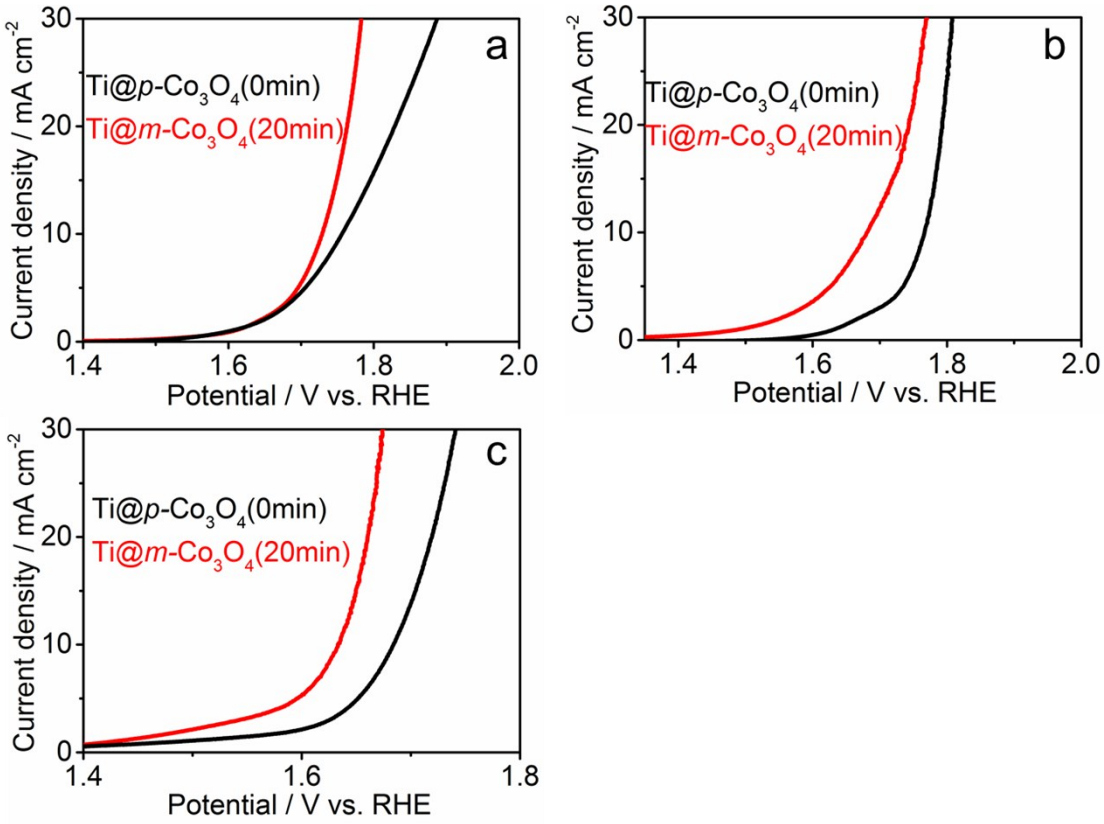


**Figure S9.** The *iR*-LSV curves of the Ti@*p*-$Co_3O_4$ (0min) and Ti@*m*-$Co_3O_4$(20min) and in $O_2$ saturated 0.5 M $H_2SO_4$ (a), 1.0 M PBS (b) and 0.1 M KOH (c) electrolytes.

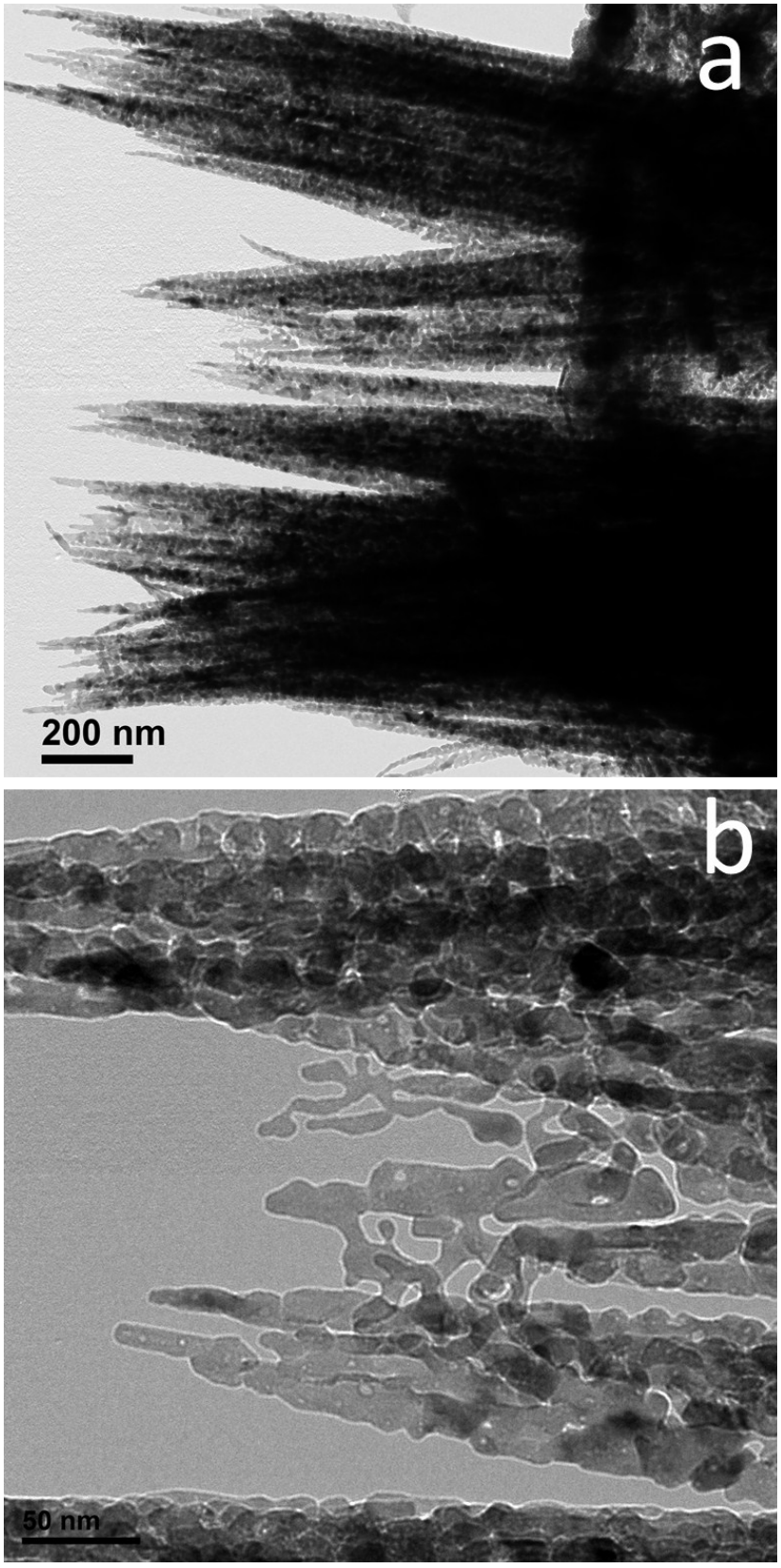


**Figure S10.** TEM images of Ti@*p*-$Co_3O_4$ nanoneedles array electrode.

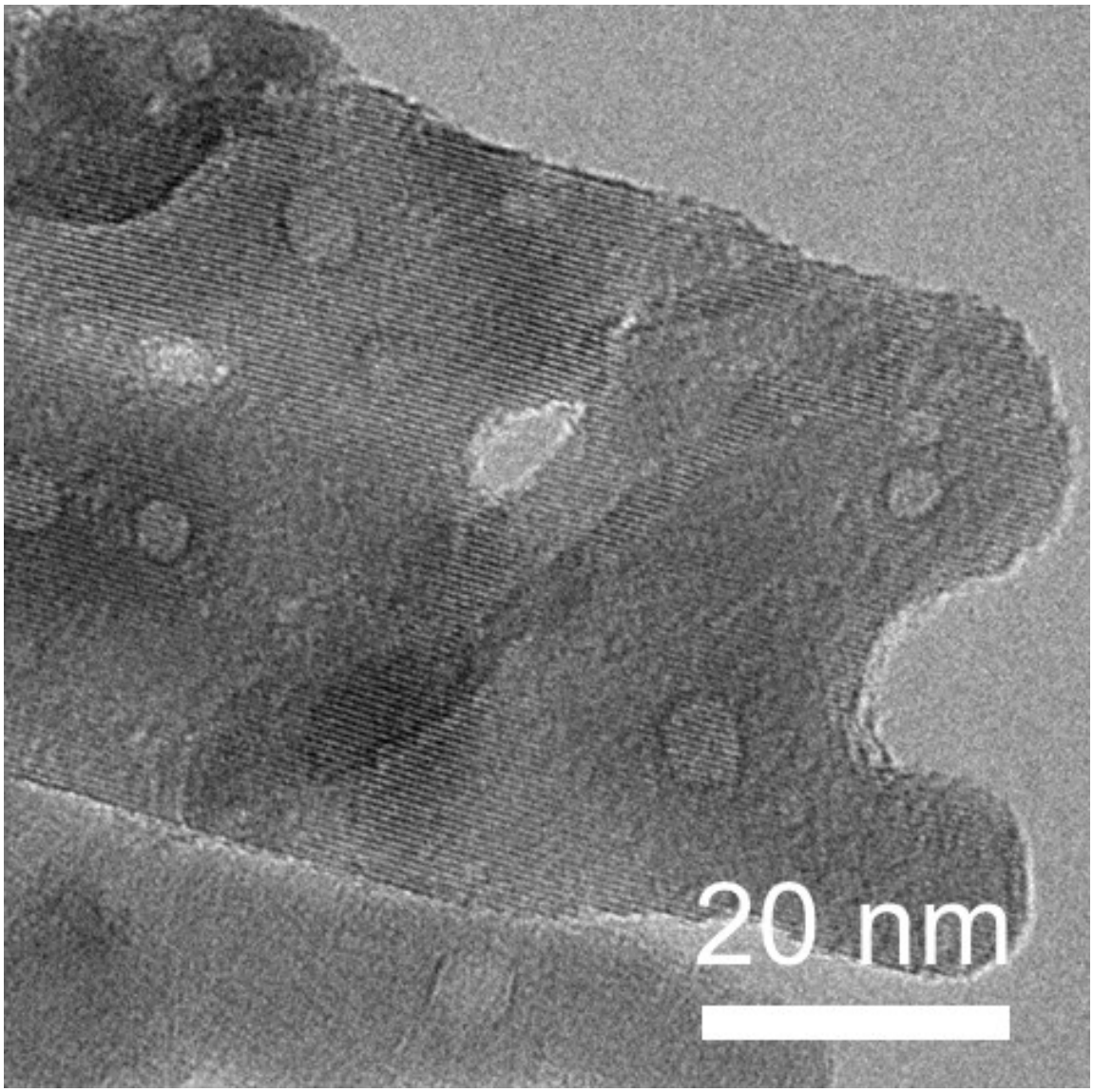


**Figure S11.** HR-TEM images of Ti@*m*-$Co_3O_4$ nanoneedles array electrode.

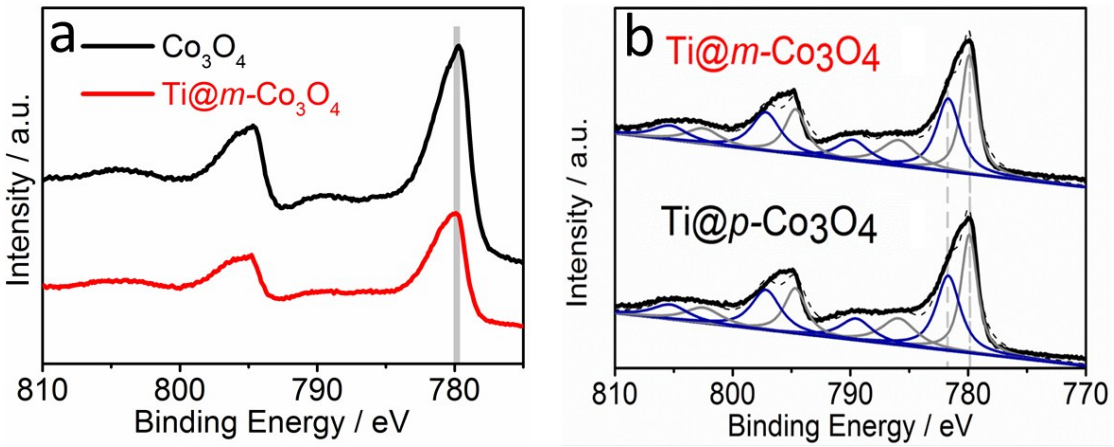


**Figure S12.** (a) The Co 2p XPS spectra of $Co_3O_4$ and Ti@*m*-$Co_3O_4$ electrodes. (b) The Co 2p XPS spectra of Ti@*m*-$Co_3O_4$ and Ti@*p*-$Co_3O_4$ electrodes. The Co2p spectra of activated Ti@*m*-$Co_3O_4$ did not find significant change compared to initial Ti@*p*-$Co_3O_4$.

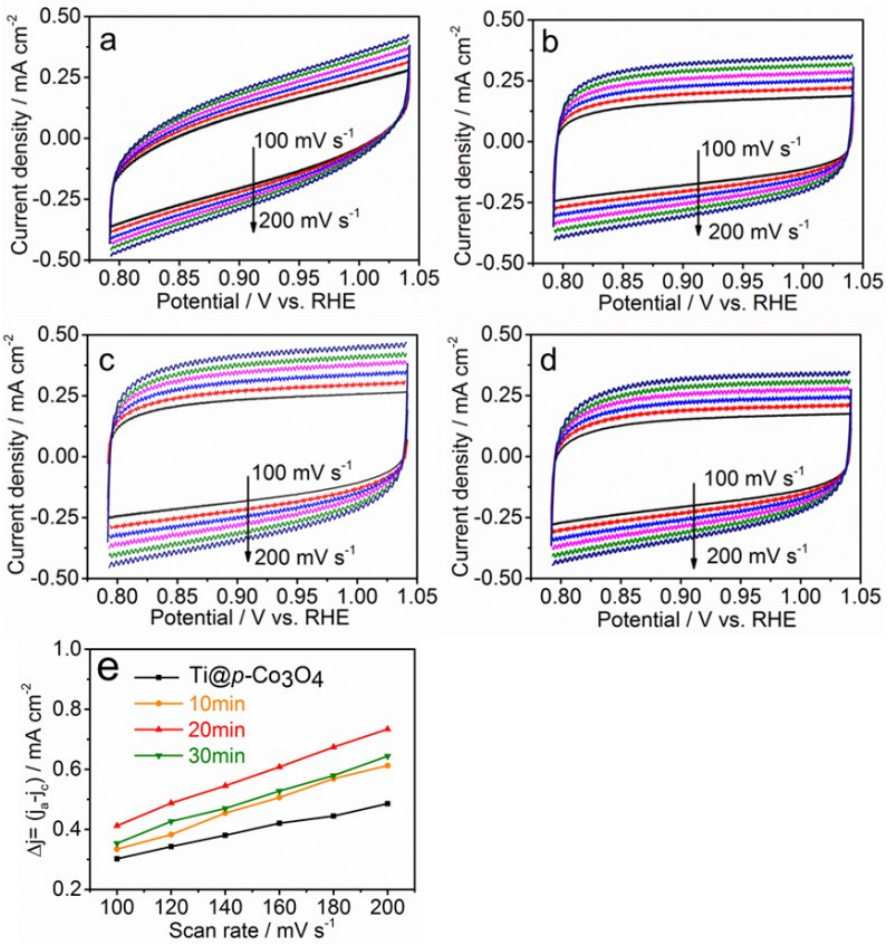


**Figure S13**. (a-d) Cyclic voltammetry (CV) curves of the Ti@*p*-$Co_3O_4$ Ti@*m*-$Co_3O_4$-x (x=, 10, 20, and 30min). (e) plots of the current density VS. scan rate for Ti@*m*-$Co_3O_4$ and Ti@*p*-$Co_3O_4$ electrodes. The optimal synthesis condition gave a material that is denoted hereafter as Ti@*m*-$Co_3O_4$, unless indicated otherwise. Meanwhile, the initial nanoneedles array, without hydrazine-treated, was recorded as Ti@*p*-$Co_3O_4$.

The electrocatalytic OER performance for the Ti@$Co_3O_4$-x was carefully investigated using a three-electrode system in neutral electrolyte (pH=7).

To gain more understanding of the superior electrocatalytic activity of Ti@*p*-$Co_3O_4$ and Ti@*m*-$Co_3O_4$-x, we further estimate the effective active surface area of the catalysts by determining the electrochemical double-layer capacitance ($C_{dl}$). The potential range with little current contribution from Faradic reaction was selected for calculating the $C_{dl}$. The final $C_{dl}$ is obtained by extracting the slope from the linear relationship of the current density difference against the scan rates. Noticeably, Ti@*m*-$Co_3O_4$ electrod shows a $C_{dl}$ of 1.6 mF $cm^{-2}$, much higher than that of Ti@*p*-$Co_3O_4$ (0.9 mF $cm^{-2}$), Ti@*m*-$Co_3O_4$-10 (1.43 mF $cm^{-2}$), and Ti@*m*-$Co_3O_4$-30 (1.405 mF $cm^{-2}$) electrodes, suggesting the high exposure of efficient active sites to boost OER process, which is accountable for the exceptional OER electrocatalytic performance.

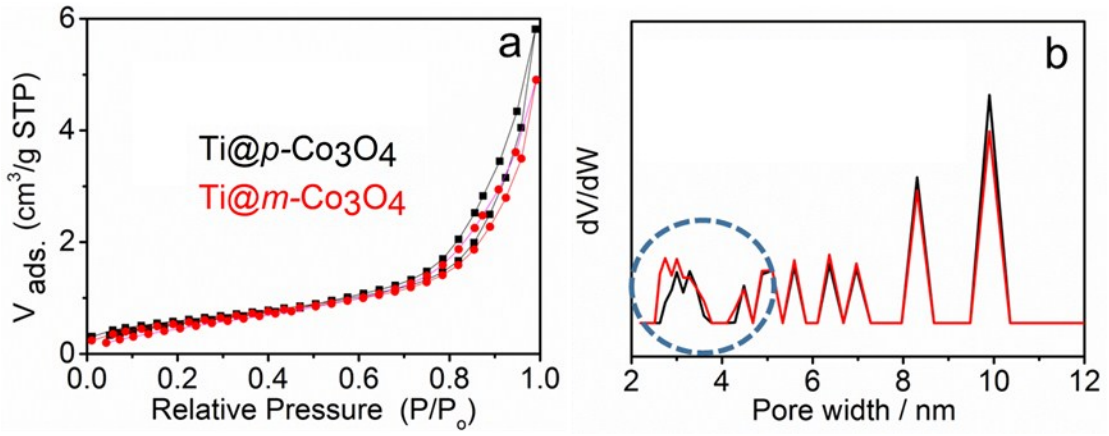


**Figure S14.** (a) Nitrogen adsorption–desorption isotherms and (b) pore width of the pristine Ti@*p*-$Co_3O_4$ and 20min hydrazine-treated Ti@*m*-$Co_3O_4$ electrodes.

In light of the excellent OER electrocatalytic performance, the polyporous and hydrazine-treated Ti@*m*-$Co_3O_4$ electrodes materials reported here with a high accessible mesopores and exposure of active sites might be promising alternatives to Ir and Ru-based OER catalysts, thus facilitating the development of the water splitting electrodes.

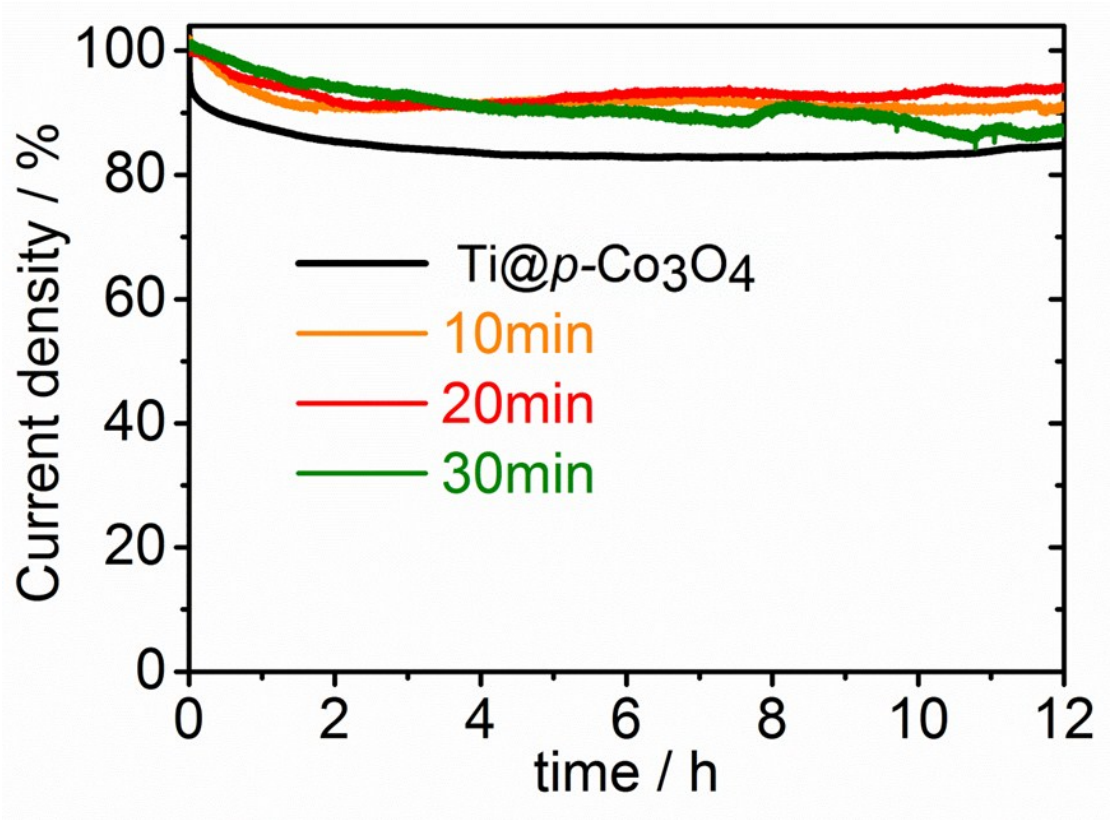


**Figure S15.** Time-dependent current density curve for the Ti@*p*-$Co_3O_4$ (0min), 10min, 20min and 30min electrodes. All experiments were carried out in 1.0 M phosphate buffer saline solution (pH = 7). The optimal synthesis condition gave a material that is denoted hereafter as Ti@*m*-$Co_3O_4$, unless indicated otherwise. Meanwhile, the initial Ti@$Co_3O_4$ nanoneedles array, without hydrazine-treated, was recorded as Ti@*p*-$Co_3O_4$.

The long-term durability of the Ti@*m*-$Co_3O_4$-x (x = 10, 20 and 30min) electrodes for OER was tested by a chronoamperometry measurement. The effect of hydrazine-treated time on the OER stability for the $Co_3O_4$ nanoneedles array was also systematically studied. The result directly demonstrates the pivotal role of hydrazine treatment with appropriate degree in maintaining the excellent catalytic stability. The Ti@*m*-$Co_3O_4$ electrode demonstrates better stability than the pristine Ti@*p*-$Co_3O_4$. The catalytic efficiency and stability problems for Ti@*m*-$Co_3O_4$ are addressed at the same time, leading to a promising future in replacing Ir and Ru-based catalysts for the OER.

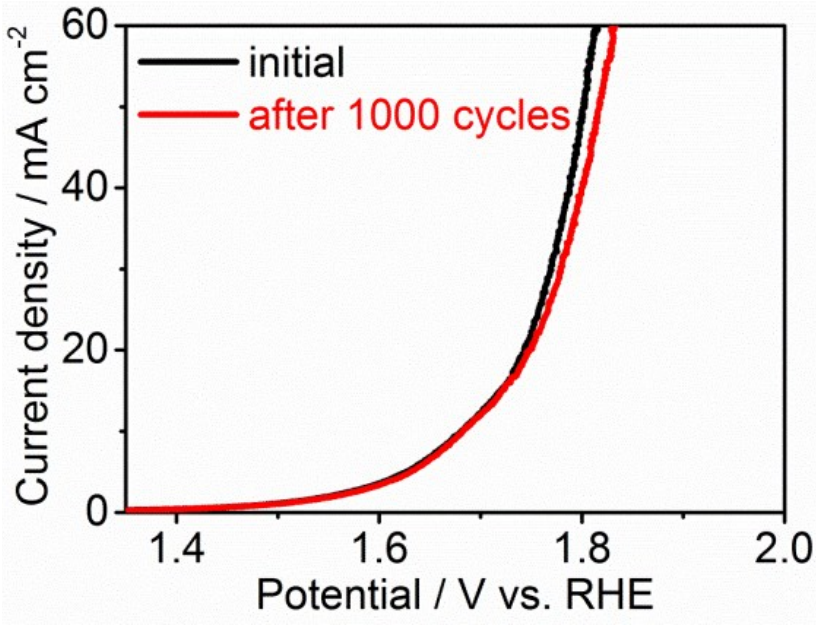


**Figure S16.** Polarization curves recorded for Ti@*m*-$Co_3O_4$ nanoneedles array electrode initial and after 1000 continuous cyclic voltammagram (CV) cycles. The optimal synthesis condition gave a material that is denoted hereafter as Ti@*m*-$Co_3O_4$, unless indicated otherwise. A remarkably high OER stability of Ti@*m*-$Co_3O_4$ electrode was well presented by the high retention ratio (94%) of the anodic current density after 12 h and the negligible loss in the current density after 1000 cyclic voltammagram (CV) cycles (Figure 4a).

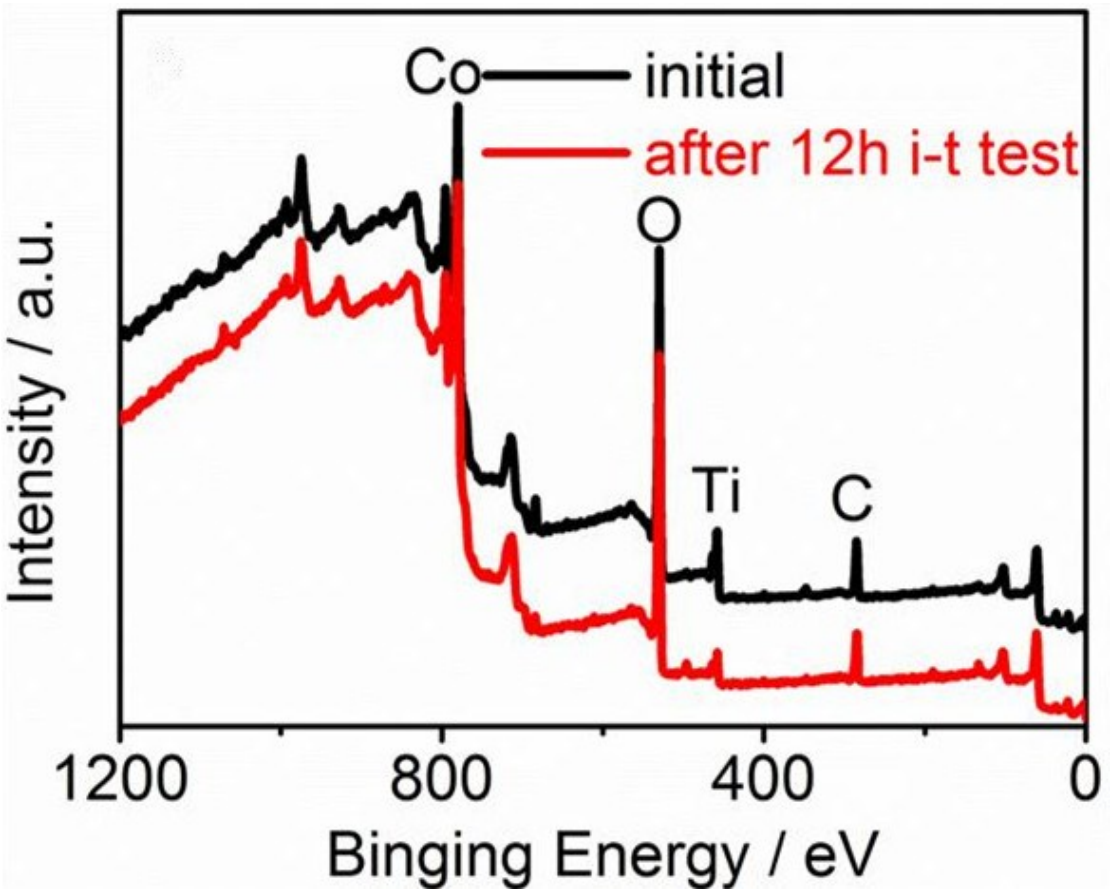


**Figure S17.** XPS survey of the Ti@*m*-$Co_3O_4$ before and after 12h stability test. X-ray photoelectron spectroscopy (XPS) measurements are performed to further confirm the chemical compositions and oxidation states of the Ti@*m*-$Co_3O_4$ before and after 12h stability test. Cobalt oxide nanoarrays anchored onto Ti mesh as an efficient OER electrode for long-life water splitting with good performance. Without polymeric binders (conductive additives), the self-standing Ti@*m*-$Co_3O_4$ electrode achieves a high current density of 49.9 mA $cm^{-2}$ even at 1.8 V vs. RHE.

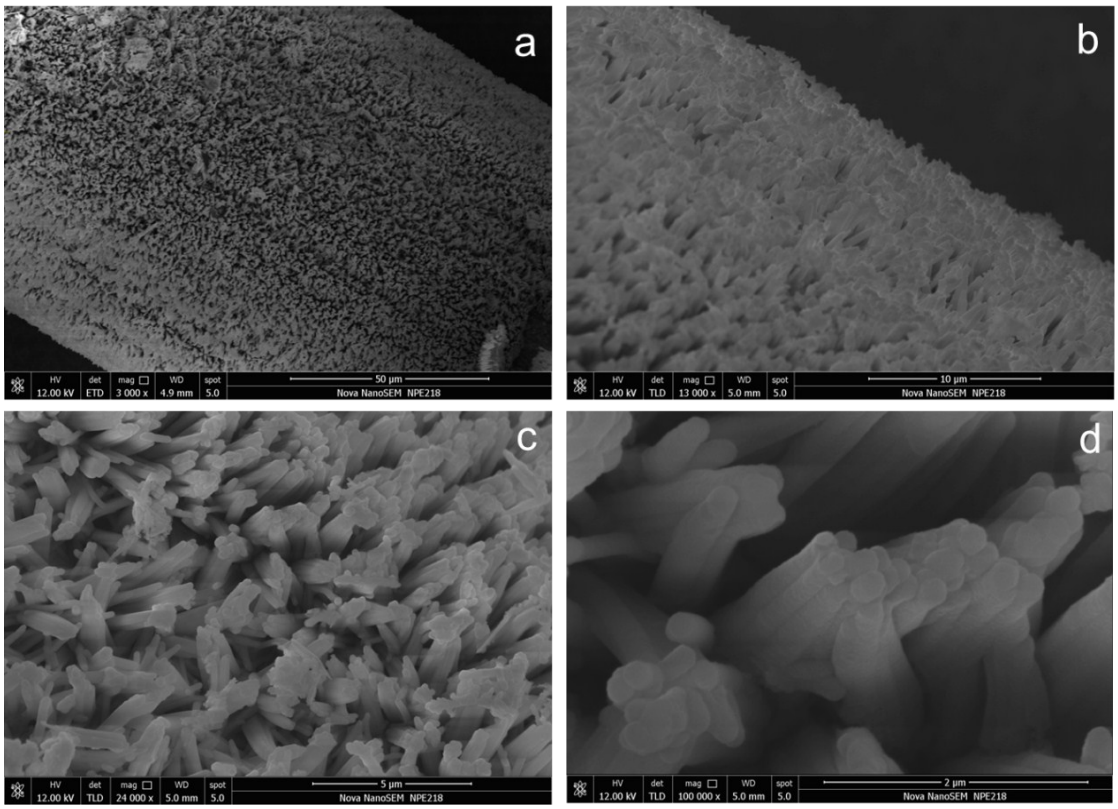


**Figure S18.** Typical SEM images the Ti@*m*-$Co_3O_4$ after 12h stability test. The optimal synthesis condition gave a material that is denoted hereafter as Ti@*m*-$Co_3O_4$, unless indicated otherwise. Benefiting from the well-designed hierarchical Ti@*m*-$Co_3O_4$ nanoarchitecture, the Ti@*m*-$Co_3O_4$ arrays anchored onto Ti mesh offer abundant porous space to allow sufficient electrolyte penetration, and facilitate the transport of ions and electrons. The binder-free, self-standing Ti@*m*-$Co_3O_4$ electrode, without conductive additives, exhibits significant improvement in the current output and long-term cycling stability. Despite the hierarchical morphology change during OER durability test, the electrochemical performance is largely consistent to the initial current output (Figure 4d).

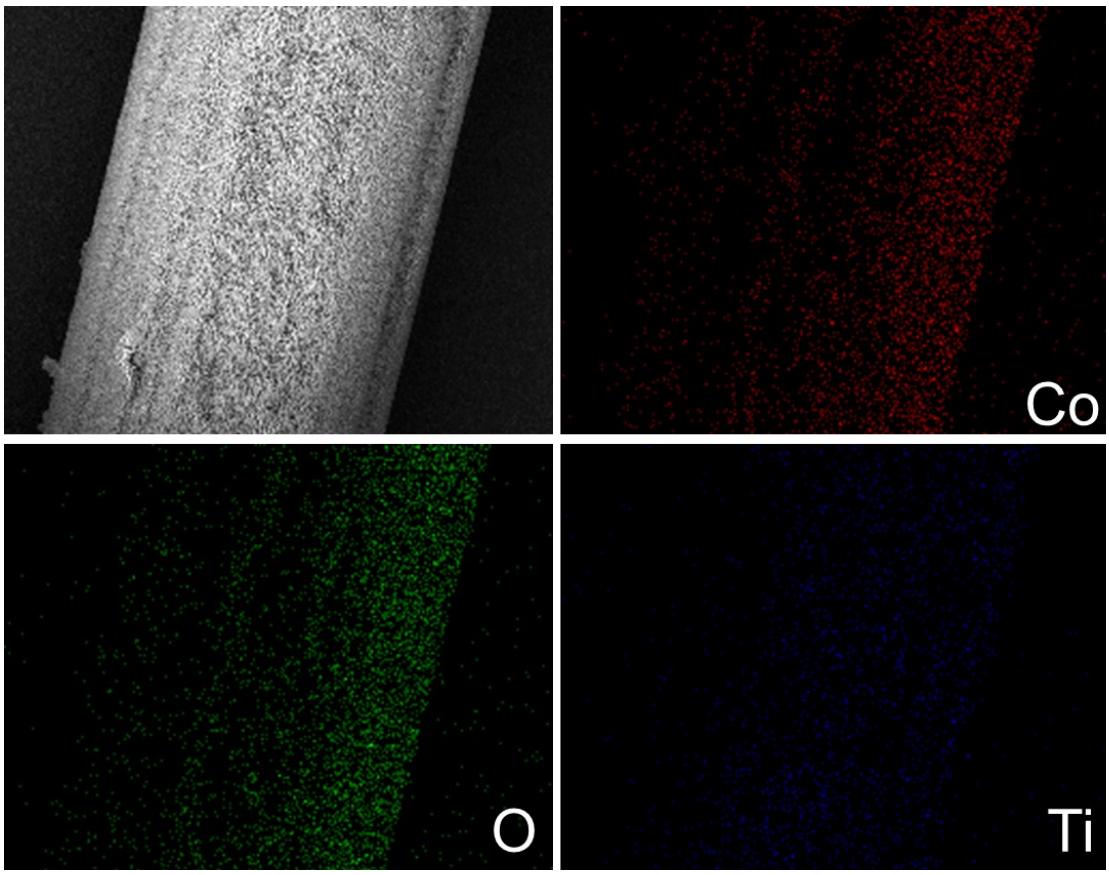


**Figure S19.** Typical EDS mapping of the Ti@*m*-$Co_3O_4$ after 12h stability test. The optimal synthesis condition gave a material that is denoted hereafter as Ti@*m*-$Co_3O_4$, unless indicated otherwise. As displayed in Figure S18, the mapping result exhibits a homogeneous distribution of the Co, O elements.


**Figure S20.** Typical TEM image the Ti@*m*-$Co_3O_4$ after 12h stability test. The optimal synthesis condition gave a material that is denoted hereafter as Ti@*m*-$Co_3O_4$, unless indicated otherwise.

The image shows that the used Ti@*m*-$Co_3O_4$ electrode tend to agglomerate after long-time stability test, which maybe decreases the exposed active interfaces and sites of nanoelectrodes.

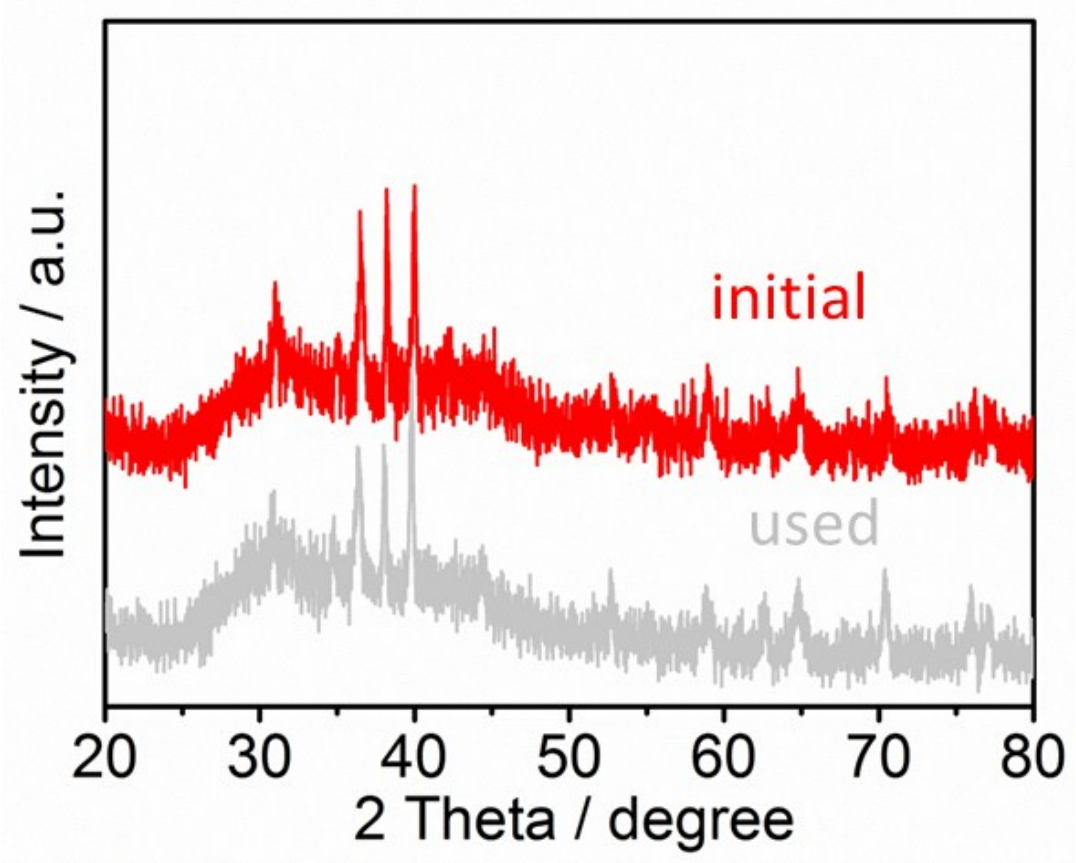


**Figure S21.** XRD of the initial Ti@*m*-$Co_3O_4$ and used after 12h stability test.
The crystalline phase of these $Co_3O_4$ nanobundles array was not disturbed obviously.

# 3.Supplementary Tables

**Table S1.** Summarized the relevant synthesis parameters of Ti@*p*-$Co_3O_4$ and Ti@*m*-$Co_3O_4$-x (10, 20, and 30min) hybrid electrodes.

| samples | $N_2H_4 \cdot H_2O + H_2O$ (15mL+5mL) / min |
|---|---|
| Ti@p-$Co_3O_4$ | 0 |
| Ti@*m*-$Co_3O_4$-10 | 10 |
| Ti@*m*-$Co_3O_4$ | 20 |
| Ti@*m*-$Co_3O_4$-30 | 30 |

**Table S2.** Comparison of OER catalytic performance for Ti@*p*-$Co_3O_4$ and Ti@*m*-$Co_3O_4$-x (10, 20, and 30min) electrocatalysts in neutral solution.

| samples | j @ 1.8V vs. RHE (mA $cm^{-2}$) | η@10mA $cm^{-2}$ (mV) |
|---|---|---|
| Ti@p-$Co_3O_4$ | 24.23 | 530 |
| Ti@*m*-$Co_3O_4$-10 | 31.83 | 506 |
| Ti@*m*-$Co_3O_4$ | 49.90 | 450 |
| Ti@*m*-$Co_3O_4$-30 | 27.72 | 486 |

The current densities at 1.8V versus reversible hydrogen electrode (RHE) and the overpotential at 10 mA $cm^{-2}$ are summarized in Table S2. The electrochemical experiments show that the Ti@*m*-$Co_3O_4$ electrode affords 49.6 milliamps per square centimeter at 1.8 V vs. RHE in 1.0 M PBS electrolyte. As expected, the Ti@*m*-$Co_3O_4$ electrode shows the best OER performance with the lowest onset potential and overpotential. This indicates the better OER performance of the Ti@*m*-$Co_3O_4$ than that other sample. This performance also outperforms that of previous many newly developed transition metal-based OER electrocatalysts in a same electrolyte (Supplementary Table S3). The much better OER performance of the Ti@*m*-$Co_3O_4$ electrode than that of the Ti@*p*-$Co_3O_4$ confirms that the treatment time of hydrazine indeed plays an important role in improving OER electrocatalytic activity.

**Table S3.** Comparison of the OER performance of well-developed electrocatalysts in neutral solution and near neutral condition.

| Catalysts | Loading ($mg/cm^2$) | j @ 1.8V (mA $cm^{-2}$) | **pH** | **η** | | Substrate/ Area ($cm^2$) | Reference |
|---|---|---|---|---|---|---|---|
| | | | | 1mA $cm^{-2}$ | 10 mA $cm^{-2}$ | | |
| **Ti@m-$Co_3O_4$** | **0.84** | **49.90** | **7** | **260** | **450** | **Ti mesh/ 3** | **This study** |
| Co-Bi NS/G | 0.27 | 14.4 | 7 | -- | 480 | GCE[a]/0.07 | s1 |
| $Co_3S_4$ nanosheets | 0.28 | 2.8 | 7 | 470 | -- | GCE/0.07 | s2 |
| Au-$Co(OH)_2$ | ---[b] | 1.6 | 7 | 410 | -- | FTO[c]/ 2 | s3 |
| $Co_3O_4$/SWNTS | 0.025 | 2.5 | 7 | 320 | 832 | ITO[d]/ 1 | s4 |
| $Co(PO_3)_2$ | 1.1 | 11 | 6.4 | -- | 605 | Ni form/ 1 | s5 |
| Iron oxyhydroxide films Fe based film | 153nmol/ $cm^2$ | 7 | 9 | 495 | 600 | ITO/ 0.27 | s6 |
| 1 D-CoHCF-90 array | 0.7 | 2.5 | 7 | 383 | -- | carbon paper/--[b] | s7 |
| $Bi_2WO_6$ plates | 0.34 | 13 | 7 | -- | 540 | GCE/0.07 | s8 |
| $Mo_5O_8$ | ---[b] | 5 | 7.8 | 550 | -- | FTO/ --[b] | s9 |
| Ni42-300 | ---[b] | 10 | 7 | 195 | 590 | Ni42 steel/4.5 | s10 |
| $X_{20}CoCrWMo_{10}$-9//$Co_3O_4$ | ---[b] | 25 | 7 | -- | 222 | X20CoCrWMo10 -9 Steel/4.8 | s11 |
| (Co-Hi) | 297 nmol/$cm^2$ | 4 | 7 | 270 | -- | FTO/1 | s12 |
| n-Co2P nanoparticles | -- | 5 | 6.86 | -- | 680 | GCE/0.196 | s13 |
| a-Co2P nanoparticles | -- | 10 | 6.86 | -- | 600 | GCE/0.196 | s13 |
| **Ni-Bi/CC** | 2.3 | 30 | 9.2 | 380 | 470 | CC/---[b] | s14 |
| **Co-Bi/Ti** | 1.2 | 38 | 9.2 | ---- | 469 | Ti / 4 | s15 |
| **Fe–Co3O4@Fe–Co–Bi/CC** | --- | 42 | 0.1 M K-Bi | | 420 | CC/8 | s16 |

[a] GCE, glassy carbon electrode; [b] Not reported; [c] FTO, Fluorine-doped tin oxide glass slide; [d] ITO, Indium tin oxide.

**Table S4:** Comparison of catalytic performances (TOF) and conditions for a variety of earth-abundant transition metals electrocatalysts in neutral solution and near neutral condition.

| Catalysts | Catalyst Loading/ nmol $cm^{-2}$ | j @ 1.8V vs. RHE (mA $cm^{-2}$) | TOF/$h^{-1}$ at corresponding Overpotential | pH values | References |
|---|---|---|---|---|---|
| Ti@m-$Co_3O_4$ | 3500 | 49.9 | 68.62 (530mV) | 7 | This study |
| Ti@m-$Co_3O_4$ | 3500 | 49.9 | 86.5(545mV) | 7 | This study |
| Ti@m-$Co_3O_4$ | 3500 | 49.9 | 152.6 (580mV) | 7 | This study |
| Fe-based | 10.2 | 2.5 | 756 (530mV) | 7 | S17 |
| Mn oxides | 80 | 1.2 | 36 (530mV) | 7 | S18 |
| Co-based | 100 | 0.4 | 61.2 (530mV) | 7 | S19 |
| Ni-based | 100 | 2.6 | 36 (530mV) | 9.2 | S20 |
| Co-Pi | 1000 | ---[a] | 10 (545mV) | 7.0 | S21 |
| $Li_2Co_2O_4$ | 276 | ---[a] | 8.5 (580mV) | 7.2 | S22 |
| nano-$MnO_2$ | ---[a] | 2.4 | 0.18(600mV) | 6 | S23 |
| $NiO_x$-en | 270 | 3.7 | 54 (610 mV) | 9.2 | S24 |
| $Mn_3(PO_4)_2$ | 611 | 0.04 | 4.4 (680 mV) | 7.0 | S25 |
| $MnO_2$-Py | 1600 | 2.25(1.6V vs. SHE)[b] | 11.3 (910 mV) | 7.5 | S26 |
| Ti@$Co_{0.85}Se$ | 522 | 29.6 | 162 (530mV) | 7 | S27 |

[a] Not reported. [b] SHE: Standard hydrogen electrode.

**Table S5.** Comparison of electrochemical double-layer capacitance ($C_{dl}$) for Ti@*p*-$Co_3O_4$ and Ti@m-$Co_3O_4$-x (x = 10, 20, 30min) electrocatalysts in neutral solution (pH = 7).

| Samples | Electrochemical double-layer capacitance ($C_{dl}$) |
|---|---|
| Ti@*p*-$Co_3O_4$ | 0.9 mF $cm^{-2}$ |
| Ti@*m*-$Co_3O_4$-10 | 1.43 mF $cm^{-2}$ |
| Ti@$Co_3O_4$ | 1.6 mF $cm^{-2}$ |
| Ti@*m*-$Co_3O_4$-30 | 1.405 mF $cm^{-2}$ |

Since electrochemical double-layer capacitance ($C_{dl}$) is proportional to the electrochemically active surface area (ECSA), cyclic voltammetry (CV) was conducted from 100 mV to 200 mV with different scan rates to estimate the ECSA. Apparently, the $C_{dl}$ of Ti@m-$Co_3O_4$ (1.6 mF $cm^{-2}$) was larger than that of Ti@p-$Co_3O_4$ (0.9 mF $cm^{-2}$), respectively. Such a large $C_{dl}$ may expose more electrochemical active area, which could contribute to the high OER performance of Ti@*m*-$Co_3O_4$ binary hybrid electrodes.

## Notes and references


[S1] P. Z Chen, K.Xu, Tianpei Zhou, Yun Tong, Junchi Wu, Han Cheng, Xiuli Lu, Hui Ding, Changzheng Wu, and Yi Xie, Strong-coupled cobalt borate nanosheets/graphene hybrid as electrocatalyst for water oxidation under both alkaline and neutral conditions, *Angew. Chem. Int. Ed.* **2016**, 55, 2488-2492, *Angew. Chem.* **2016**, 128, 2534-2538

[S2] Y. W. Liu, C. Xiao, M. J. Lyu, Y. Lin, W. Z. Cai, P. C. Huang, W. Tong, Y. M. Zou, and Y. Xie, Ultrathin $Co_3S_4$ nanosheets that synergistically engineer spin states and exposed polyhedra that promote water oxidation under neutral conditions, *Angew. Chem. Int. Ed.* **2015**, 54, 11231-11235; *Angew. Chem.* **2015**, 127, 11383-11387

[S3] Y. Zhang, B. Cui, Z. Qin, H. Lin, J. Li, Hierarchical wreath-like Au–$Co(OH)_2$ microclusters for water oxidation at neutral pH, *Nanoscale*, **2013**, 5, 6826-6833

[S4] J. Wu, Y. Xue, X. Yan, W. Yan, Q. Cheng, Y. Xie, $Co_3O_4$ nanocrystals on single-walled carbon nanotubes as a highly efficient oxygen-evolving catalyst, *Nano Res.* **2012**, 5, 521-530.

[S5] H. S. Ahn, T. D. Tilley, Electrocatalytic water oxidation at neutral pH by a nanostructured $Co(PO_3)_2$ anode, *Adv. Funct. Mater.* **2013**, 23, 227-233

[S6] D. Roy Chowdhury, L. Spiccia, S. S. Amritphale, A. Paul and A. Singh, A robust iron oxyhydroxide water oxidation catalyst operating under near neutral and alkaline conditions, *J. Mater. Chem. A*, **2016**, 4, 3655-3660

[S7] H. T. Bui, D. Y. Ahn, K. Shrestha, M. M. Sung, J. K. Leeb and S. H. Han, Self-assembly of cobalt hexacyanoferrate crystals in 1-D array using ion exchange transformation route for enhanced electrocatalytic oxidation of alkaline and neutral water, *J. Mater. Chem. A*, **2016**, 4, 9781-9788

[S8] Z. P. Nie, D. K. Ma, G. Y. Fang, W. Chena and S. M. Huang, Concave $Bi_2WO_6$ nanoplates with oxygen vacancies achieving enhanced electrocatalytic oxygen evolution in near-neutral water, *J. Mater. Chem. A*, **2016**, 4, 2438-2444.

[S9] D. Jeong, K. Jin, S. E. Jerng, H. Seo, D. Kim, S. H. Nahm, S. H. Kim, and K. T. Nam, $Mn_5O_8$ nanoparticles as efficient water oxidation catalysts at neutral pH, *ACS Catal.* **2015**, 5, 4624-4628.

[S10] Helmut Schäfer, Electro-oxidation of Ni42 steel: a highly active bifunctional electrocatalyst, *Adv. Funct. Mater.* **2016** ,26, 6402-6417

[S11] Helmut Schäfer, $X_{20}CoCrWMo_{10-9}//Co_3O_4$: a metal–ceramic composite with unique efficiency values for water-splitting in the neutral regime, *Energy Environ. Sci.,* **2016**, 9, 2609-2622

[S12] H. Chen, Y. Gao, and L. C. Sun, Cobalt-Based Film for Highly Efficient Electrocatalytic Water Oxidation in Neutral Aqueous Solution, *ChemCatChem* **2016**, 8, 2757-2760.

[S13] Kun Xu, Han Cheng, Linqi Liu, Haifeng Lv, Xiaojun Wu, Changzheng Wu, and Yi Xie, Promoting Active Species Generation by Electrochemical Activation in Alkaline Media for Efficient Electrocatalytic Oxygen Evolution in Neutral Media, *Nano Lett.*, **2017**, 17, 578-583.

[S14] Xuqiang Ji, Liang Cui, Danni Liu, Shuai Hao, Jingquan Liu, Fengli Qu, Yongjun Ma, Gu Du, Abdullah M. Asiri, and Xuping Sun, A nickel-borate nanoarray: a highly active 3D oxygen-evolving catalyst electrode operating in near-neutral water, Chem. Commun., 2017, 53, 3070-3073.

[S15] Libin Yang, Danni Liu, Shuai Hao, Rongmei Kong, Abdullah M. Asir, Chengxiao Zhang, and Xuping Sun, A cobalt-borate nanosheet array: an efficient and durable non-noble-metal electrocatalyst for water oxidation at near neutral pH, J. Mater. Chem. A, 2017, 5, 7305-7308.

[S16] Guilei Zhu, Ruixiang Ge, Fengli Qu, Gu Du, Abdullah M. Asiri logoe, Yadong Yao and Xuping Sun, In situ surface derivation of an Fe–Co–Bi layer on an Fe-doped $Co_3O_4$ nanoarray for efficient water oxidation electrocatalysis under near-neutral conditions, J. Mater. Chem. A, 2017, 5,

6388-6392.
[S17] Y. Wu, M. X Chen, Y. Z Han, H. X. Luo, X. J Su, M. T. Zhang, X. h. Lin, J. L. Sun, L. Wang, L. Deng, W. Zhang, and R. Cao, Fast and simple preparation of iron-based thin films as highly efficient water-oxidation catalysts in neutral aqueous solution, *Angew. Chem. Int. Ed.* **2015**, 54, 4870-4875; *Angew. Chem.* **2015**, 127, 4952-4957
[S18] I. Zaharieva, P. Chernev, M. Risch, K. Klingan, M. Kohlhoff, A. Fischer and H. Dau I. Zaharieva, P. Chernev, M. Risch, K. Klingan, M. Kohlhoff, A. Fischer, H. Dau, Electrosynthesis, functional, and structural characterization of a water-oxidizing manganese oxide, *Energy Environ. Sci.* **2012**, 5, 7081-7089.
[S19] Matthew W. Kanan and Daniel G. Nocera, In situ formation of an oxygen-evolving catalyst in neutral water containing phosphate and $Co^{2+}$, *Science* **2008**, 321, 1072-1075.
[S20] M. Dinca˘, Y. Surendranath, D. G. Nocera, Nickel-borate oxygen-evolving catalyst that functions under benign conditions, *Proc. Natl. Acad. Sci.* **2010**, 107, 10337-10341.
[S21] S. Cobo, J. Heidkamp, P. A. Jacques, J. Fize, V. Fourmond, L. Guetaz, B. Jousselme, V. Ivanova, H. Dau, S. Palacin, M. Fontecave, V. Artero, A Janus cobalt-based catalytic material for electro-splitting of water, *Nat. Mater.* **2012**, 11, 802-807.
[S22] G. P. Gardner, Y. B. Go, D. M. Robinson, P. F. Smith, J. Hadermann, A. Abakumov, M. Greenblatt, G. C. Dismukes, Structural requirements in lithium cobalt oxides for the catalytic oxidation of water, *Angew. Chem. Int. Ed.* **2012**, 51, 1616– 1619; *Angew. Chem.* **2012**, 124, 1648-1651.
[S23] M. Fekete, R. K. Hocking, S. L. Y. Chang, C. Italiano, A. F. Patti, F. Arena and L. Spiccia, Highly active screen-printed electrocatalysts for water oxidation based on β-manganese oxide, *Energy Environ. Sci.,* **2013**, 6, 2222-2232
[S24] A. Singh, S. L. Y. Chang, R. K. Hocking, U. Bach, L. Spiccia, Highly active nickel oxide water oxidation catalysts deposited from molecular complexes, *Energy Environ. Sci.* **2013**, 6, 579-586.
[S25] K. Jin, J. Park, J. Lee, K. D. Yang, G. K. Pradhan, U. Sim, D. Jeong, H. L. Jang, S. Park, D. Kim, N. E. Sung, S. H. Kim, S. Han, K. T. Nam, Hydrated manganese(II) phosphate ($Mn_3(PO_4)_2 \cdot 3H_2O$) as a water oxidation catalyst, *J. Am. Chem. Soc.* **2014**, 136, 7435-7443.
[S26] A. Yamaguchi, R. Inuzuka, T. Takashima, T. Hayashi, K. Hashimoto, R. Nakamura, Regulating proton-coupled electron transfer for efficient water splitting by manganese oxides at neutral pH, *Nat. Commun.* **2014**, 5, 4256-4261.
[S27] Jun-Jun Zhang, Hui Su, Hong-Hui Wang, Zhong-Hua Xue, Bing Zhang, Xiao Wei, Xin-Hao Li, Shin-Ichi Hirano, and Jie-Sheng Chen, Constructing Ohmic Contact in Cobalt Selenide/Ti Dyadic Electrode: the Third Aspect to Promote the Oxygen Evolution Reaction, *Nano Energy* **2017,** 39, 321-327.